Dark-state phase transition to a dark soliton in a dissipative Bose-Hubbard chain

Robbe Ceulemans [1,*] Samuel E. Begg [2,3,4,†] Matthew J. Davis [5,‡] and Michiel Wouters [1,§]

[1]*TQC, Departement Fysica, Universiteit Antwerpen, B-2000 Antwerpen, Belgium*

[2]*Department of Physics, Oklahoma State University, Stillwater, Oklahoma 74078, USA*

[3]*Asia Pacific Center for Theoretical Physics, Pohang 37673, South Korea*

[4]*Department of Physics, The University of Texas at Dallas, Richardson, Texas 75080, USA*

[5]*Australian Research Council Centre of Excellence in Future Low-Energy Electronics Technologies, School of Mathematics and Physics, University of Queensland, St Lucia, Queensland 4072, Australia*

(Received 14 November 2025; revised 19 March 2026; accepted 2 July 2026; published 6 August 2026)

We show that a Bose-Hubbard model with local loss exhibits a first-order dark-state phase transition between a dark soliton and a uniform superfluid. Semiclassical simulations and stability analysis reveal that the soliton acts as a many-body dark state, whose suppressed fluctuations modify the transition relative to the comparable phenomenon of optical bistability in Kerr resonators. This mechanism quantitatively captures the bistable phase boundary observed in the experiment of Labouvie *et al.* [Phys. Rev. Lett. **116**, 235302 (2016)], resolving long-standing discrepancies in previous theoretical modeling. Our results identify a general route by which spatial coherence and engineered loss can generate nonequilibrium phase transitions in ultracold gases.

DOI: 10.1103/dv77-31g7

I. INTRODUCTION

While dissipation is often seen as a nuisance for quantum systems, engineered dissipation can stabilize coherent many-body states and even drive nonequilibrium phenomena [1–4]. Prominent experimental examples include exciton-polariton condensation [5], a Mott insulator of photons [6], and the Mott-superfluid transition via engineered two-body loss in cold atoms [7]. This has opened a frontier for investigating the role of quantum fluctuations in driven-dissipative phase transitions [8,9], and has highlighted that states that effectively decouple from the environment—*dark states* [10,11]—can lead to phenomena such as absorbing state phase transitions [12–14] and nonequilibrium quantum critical dynamics [15–17]. A canonical, first-order phase transition is given by the so-called "optical bistability" in driven-dissipative Kerr resonators [18], where switches between macrostates can be induced by quantum fluctuations [19]. Analogous transitions have been explored in a variety of platforms [20–24].

In this work, we demonstrate a first-order dark-state phase transition between a dark soliton and a uniform superfluid in a dissipative Bose-Hubbard (BH) model [Fig. 1(a)]. A dark soliton is an excited eigenmode of the Gross-Pitaevskii equation characterized by a π-phase slip and vanishing density at its core, which allows the state to decouple from locally engineered loss there. The transition between the uniform state and the soliton arises from the competition between coherent refilling and depletion by loss. While it resembles optical bistability in Kerr resonators, the soliton's spatial phase texture and dark-state character strongly suppress fluctuations and shift the critical point.

Using semiclassical field models, we show that this phase transition quantitatively captures the bistability phase boundary observed in recent cold-atom experiments [24–26]. In those experiments, hysteresis curves are constructed from site-resolved density measurements under parameter sweeps, without determining the phase of the sites. The microscopic identity of the low-density state in the observed hysteresis loops, and the mechanism fixing the location of the phase boundary, therefore remained unresolved by prior first-principles modeling [24–28].

Beyond the implications for experiments, our work identifies a distinct nonequilibrium critical phenomenon driven by the interplay of quantum coherence and dissipation. This complements a growing body of work that uses local loss as a tool for controlling quantum transport [29–45] and for preparing far-from-equilibrium superfluid states with exotic relaxation [46–50].

II. DARK-STATE PHASE TRANSITION

We consider a one-dimensional (1D) BH chain of integer length $L+1$ subject to Markovian dissipation [51] in the form of single-particle loss on the central site ($j=0$) at rate γ, with $j \in \{-L/2, L/2\}$ the lattice index, as pictured in Fig. 1(a). In the semiclassical limit, the field amplitude ψ_j for $j \neq 0$ obeys [28]

$$i\hbar\partial_t \psi_j = \mathcal{H}\psi_j - J(\psi_{j-1} + \psi_{j+1}), \tag{1}$$

*Contact author: robbe.ceulemans@uantwerpen.be
†Contact author: samuel.begg@utdallas.edu
‡Contact author: mdavis@uq.edu.au
§Contact author: michiel.wouters@uantwerpen.be

Published by the American Physical Society under the terms of the Creative Commons Attribution 4.0 International license. Further distribution of this work must maintain attribution to the author(s) and the published article's title, journal citation, and DOI.

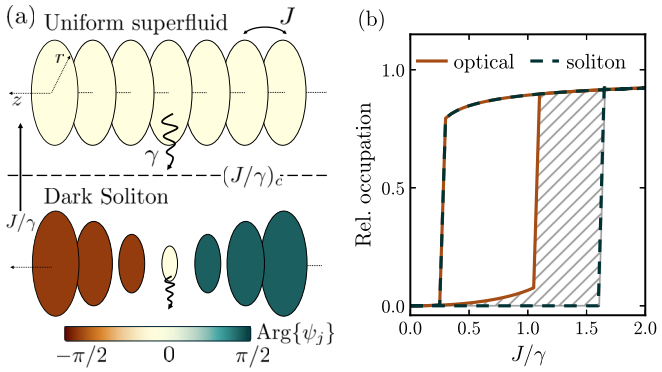

FIG. 1. (a) Illustration of the two late-time macrostates in a quasi-1D Josephson junction chain with tunneling J and local particle loss γ on the central site. As J/γ increases, there is a phase transition from a *dark soliton* (bottom) to a uniform superfluid (top). The former is characterized by a π-phase jump and vanishing density on the central site, and is a dark state that decouples from the dissipation. (b) Central-site occupation $|\psi_0|^2$ (normalized by maximum occupation N_f) vs J, showing the bistability of numerical mean-field solutions. Dashed lines (green) show the case of a superfluid to dark soliton, which sweeps a bigger area than a comparable transition connecting the superfluid to a symmetric low-density state without π-phase jump (orange).

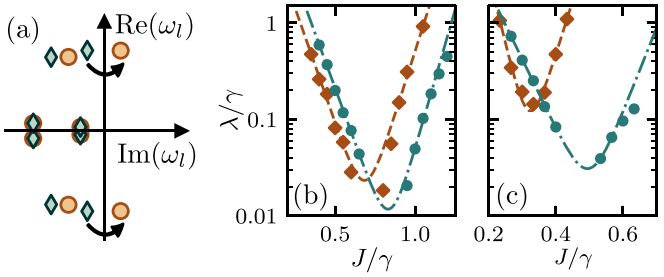

FIG. 2. (a) Linear-stability eigenvalues of the discrete dark soliton (3) in the BH chain for $J/\gamma = 0.97$ (green) and $J/\gamma = 1.06$ (orange). Effective Liouvillian gap λ as a function of J/γ at fixed dissipation rates (b) $\gamma/\mu = 0.1$ and (c) $\gamma/\mu = 0.3$. Results with the soliton (green dots) are compared to those obtained with imposed mirror-symmetry (orange diamonds), which excludes the possibility of a soliton. Broken lines are fits to guide the eye. Simulations were performed with a fixed particle number per site and L large enough to avoid boundary effects.

while for $j = 0$ the dissipative stochastic evolution is

$$i\hbar\partial_t\psi_0 = (\mathcal{H} - i\gamma/2)\psi_0 - J(\psi_{-1} + \psi_1) + \sqrt{\gamma/2}\,\eta, \quad (2)$$

with tunneling amplitude J and where $\mathcal{H}\psi_j = U|\psi_j|^2\psi_j$ describes the on-site interactions with an effective strength U. The complex Gaussian noise η satisfies $\langle\eta(t)\rangle = 0$ and $\langle\eta(t)\eta^*(t')\rangle = \delta(t - t')$.

Balancing of tunneling against local loss yields a quasi-steady state at the lossy site. For weak tunneling, $J/\gamma \ll 1$, losses dominate and the central site settles in a "normal" (quantum Zeno) state with low occupation and condensate fraction. In contrast, at large J/γ, a superfluid state emerges with the lossy site fully occupied. In the thermodynamic limit $N_j \propto N \to \infty$ (fixed γ/μ), these regimes are separated by a first-order transition at $(J/\gamma)_c$ [28], accompanied by hysteresis and bistability.

Most previous analyses interpreted the state on the low-density branch of the hysteresis curve [Fig. 1(b)] as lacking spatial phase structure, in analogy with optical bistability in a single, laser-driven cavity (Kerr resonator) [24–28,34]. By analyzing the quasi-steady states and their stability, we demonstrate that the lower branch is a dark soliton, uncovering the microscopic mechanism that fixes the observed phase boundary.

A discrete dark soliton has the characteristic spatial profile [52]

$$\psi_j = \sqrt{N_f}\tanh[jd_z/\sqrt{2\xi^2}], \quad (3)$$

where d_z is the lattice spacing, N_f is the population of a full site, and $\xi = \sqrt{Jd_z^2/\mu}$ is the soliton's healing length. It exhibits a π-phase jump and vanishing density at the central site [Fig. 1(a)], such that $\psi_0 = 0$ and the local loss term in Eq. (2) vanishes. The profile is also an eigenmode of the discrete 1D Gross-Pitaevskii equation. Consequently, the soliton (3) decouples from the bath and is therefore a dark state in the mean-field limit of Eqs. (1) and (2).

The dark-state fixed point exists for all parameters, but its dynamical stability depends on J and γ. The resulting stability structure underlies the mean-field hysteresis illustrated in Fig. 1(b). There, the hatched region highlights the larger area swept by the soliton hysteresis loop compared to a Kerr-like, phase-uniform low-density branch. The lower branch of the soliton bistability features a sudden jump from zero (dark soliton) to a finite population at a threshold value $J = J_t$ (for a fixed γ/μ), in keeping with a first-order phase transition. The semiclassical transition, where quantum fluctuations are ignored, therefore corresponds to a first-order dark-state phase transition, driven by a change in the stability of a dark state [9,12–14].

To probe the stability of the dark soliton, we analyze the Bogoliubov spectrum in the $N \to \infty$ limit where the noise (dissipative and vacuum) vanishes; see Appendix B for the linear stability analysis methodology. Figure 2(a) shows the complex eigenvalues for the two regimes. For $J < J_t$ (green), all eigenvalues ω_l satisfy $\mathrm{Re}\,\omega_l < 0$, implying damped excitations and a stable soliton fixed point. For $J > J_t$ (orange), a pair of complex eigenvalues crosses the real axis, indicating the onset of dynamical instability of the dark state. This signifies a *Hopf bifurcation*, in contrast to the saddle-node bifurcations characteristic of optical bistability [23]. We find no stable limit cycle for $J > J_t$, indicating a subcritical Hopf bifurcation and relaxation to the stable uniform superfluid. The finite real part of the unstable eigenvalues implies an *oscillatory* instability, as is typical of on-site solitons in 1D discrete lattices [52,53].

Quantum corrections to the perfect dark state vanish as $O(1/N)$ (see Appendix A), leaving observable signatures in large but finite systems. To include vacuum and dissipative noise at finite atom numbers, we perform truncated Wigner approximation (TWA) simulations based on Eqs. (1) and (2). The basic method and derivations are provided in Appendix A. While noise smooths the first-order transition [19,21], the extended hysteresis region persists. Individual

Wigner trajectories exhibit stochastic switching between the dark soliton and the uniform superfluid. By extracting the characteristic switching time τ from large ensembles of trajectories, we estimate the Liouvillian gap $\lambda = 1/\tau$ [28]. This switching behavior was inferred experimentally for a comparable superfluid system in Ref. [25].

Figures 2(b) and 2(c) display the Liouvillian gap λ as a function of the tunneling parameter J at fixed dissipation rates (green). Results are also displayed with enforced mirror symmetry around the central site (orange), which prohibits soliton formation and instead yields a conventional optical bistability. The minimum gap provides the best estimate of the critical point $J = J_c$. For the soliton-superfluid transition, the gap is smaller, indicating reduced fluctuations. Switching is slower because the transition requires a collective π-phase flip of an entire reservoir, whereas in optical bistability, switches are driven by dynamic noise or drive-induced, single-site fluctuations. The soliton bistability therefore requires stronger fluctuations, as occur at larger values of J.

The difference between the simulations with and without a soliton increases as the loss rate γ grows, as shown by the minima in Fig. 2(c), reflecting the increased stability of the soliton. The curve also broadens significantly, signaling an extended region of critical slowing down. In contrast, optical bistability exhibits a closing of this region with increasing γ [27,54]. Consistently, Figs. 4(a) and 4(b) demonstrate broadening of the bistable region in the γ-J plane at larger loss rates only for the soliton case [Fig. 4(a)].

III. APPLICATION TO EXPERIMENT

We now demonstrate that the soliton dark-state phase transition quantitatively explains recent experimental observations in superfluid arrays with a single lossy site [24–26,46]. These experiments were performed with ultracold rubidium in a quasi-1D chain, where each site still has substantial radial extent determined by a two-dimensional (2D) isotropic harmonic trap in the x-y plane with frequency ω_r [Fig. 1(a)]. The discrete lattice is oriented in the z direction, and the central site is subject to an electron beam [55,56] that introduces a controllable atom loss rate γ [29].

Typical atom numbers are $\mathcal{O}(10^3)$ particles per site, such that we are able to approximate the dynamics using classical fields $\psi_j(\boldsymbol{x}, t)$ evolving under coupled stochastic Gross-Pitaevskii equations [58–60]. In the TWA, time evolution of these fields is governed again by Eqs. (1) and (2), but with

$$\mathcal{H}\psi_j = \mathcal{P}\left\{\left[-\frac{\hbar\nabla^2}{2m} + V(\boldsymbol{x}) + g_2|\psi_j|^2\right]\psi_j\right\}, \tag{4}$$

where $V(\boldsymbol{x}) = \frac{1}{2}m\omega_r^2(x^2 + y^2)$ and g_2 is the 2D interaction strength. The projection operator $\mathcal{P}$ imposes a cutoff that we use to restrict the numerics to modes at relevant energies; see Ref. [59] and Appendix D for details. The complex Gaussian noise η then satisfies $\langle\eta(\boldsymbol{x}, t)\eta^*(\boldsymbol{x}', t')\rangle = \delta_C(\boldsymbol{x}, \boldsymbol{x}')\delta(t - t')$, where δ_C acts like the Dirac delta on the projected space [59]. For a single experimental run, the system is initialized in its ground state. This is taken as the "full" initial condition. The "empty" initial condition is prepared by subsequently removing atoms from the central site using an electron beam. During this preparation stage, the two halves of the system

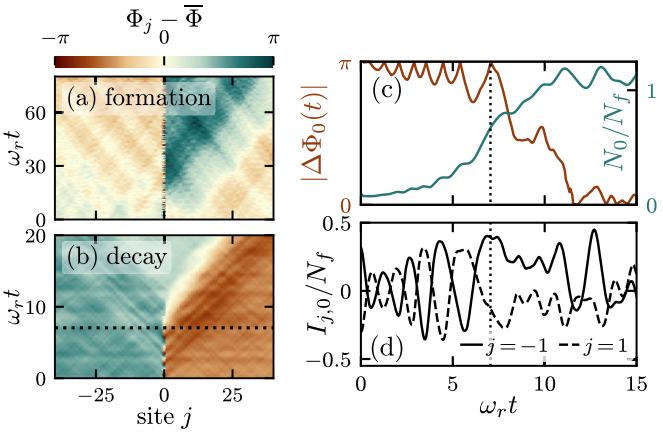

FIG. 3. Emergence and stability of a dark soliton in the experimental system. (a) Evolution of the spatial phase profile Φ_j vs time for a single trajectory with $L = 100$ (outer sites not shown), $|\Delta\Phi_0(0)| \approx 0.7$, and all sites initially full, setting $\gamma/\mu = 0.056$ and $J/\mu = 0.007$. A global phase $\bar{\Phi}$ is subtracted at each time for ease of visualization [57]. (b) As for panel (a) but starting from the soliton with initial $\Delta\Phi_0(0) \approx \pi$ and low occupation on the lossy site, setting $\gamma = 0$ and $J/\mu = 0.08$. (c) Phase difference between driving sites $|\Delta\Phi_0(t)|$ (left axis) and normalized atom number N_0/N_f on the lossy site (right axis) vs time for the trajectory in panel (b). (d) Corresponding time evolution of the current contributions from the respective driving sites, $I_{1,0}$ (dashed) and $I_{-1,0}$ (solid).

are disconnected and can drift out of phase. We approximate this effect by multiplying one half-chain by a random phase $e^{i\phi}$ (see Appendix D), a method used in Ref. [50] to obtain quantitative agreement with a comparable experiment [46] focused on the dissipationless ($\gamma = 0$) case.

We first demonstrate the emergence of the soliton for the experimental system. It has been argued that in the TWA formalism an individual trajectory is analogous to an individual experimental run [59]. Figure 3(a) shows the evolution of the phase at each site Φ_j for an example single Wigner trajectory with strong dissipation. The initial state has all sites full and the phase difference between driving sites $|\Delta\Phi_0| = |\Phi_1 - \Phi_{-1}| \ll \pi$ [61]. It can be seen that the system quickly relaxes to the soliton state with a π-phase difference from left to right.

Next, we demonstrate that despite the system's significant radial size, it is the 1D oscillatory instability of the dark soliton that sets the relevant timescale. Figure 3(b) shows the evolution of the phase Φ_j at each site for a single trajectory starting from a dark soliton state but with no dissipation ($\gamma = 0$). The corresponding evolution of the phase difference $|\Delta\Phi_0|$ and the atom number on the lossy site, N_0, are displayed in Fig. 3(c). The phase difference remains near π until the time t_r at which the occupation has grown significantly (dotted line). Around t_r, the location of the π-phase jump becomes unstable and propagates ballistically in a spontaneously chosen direction, seeded by quantum noise, leading to phase resynchronization. The robustness of a solitonlike excitation up to time t_r is consistent with the slow change in atom number compared to cases with smaller phase differences, as shown in Ref. [50]. The change in occupation over time is

$$\partial_t N_j = 2J/\hbar(I_{j+1,j} + I_{j-1,j}), \tag{5}$$

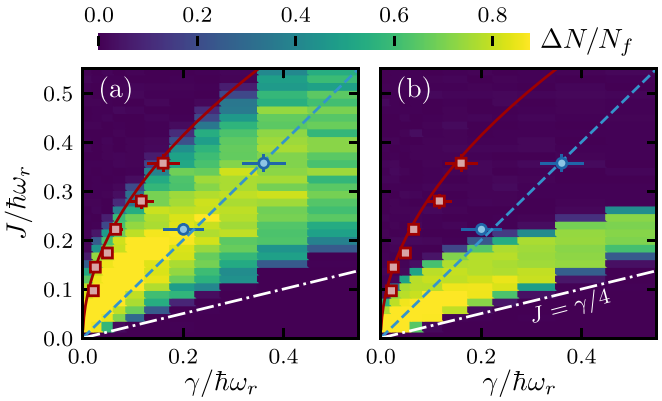

FIG. 4. (a) Phase diagram in J-γ parameter space, presented by the late-time (normalized) atomic population difference ΔN between simulations starting from different initial states: the empty and full central site, respectively. A finite ΔN indicates a bistable regime. The experimental phase boundaries from Ref. [24] are displayed with points and are fitted by $J \sim \sqrt{\gamma}$ (upper boundary) and $J \sim \gamma$ (lower boundary). The white dash-dotted line indicates $J = \gamma/4$ as expected from theory. (b) As in panel (a) but for a system with imposed mirror symmetry around the central site, which is incapable of hosting a dark soliton. Displayed data correspond to $t = 80$ ms and 251 lattice sites, averaged over 64 trajectories for each point.

where $I_{k,j} \equiv \mathrm{Im}[\langle\psi_k|\psi_j\rangle]$ denotes the current flowing between sites j and k. Figure 3(d) shows the time evolution of the current contributions from the respective driving sites, $I_{-1,0}$ and $I_{1,0}$. While the total current remains small for some time, indicated by the slowly changing atom number in Fig. 3(c), the contributions from the left and right driving sites oscillate with approximately equal magnitude but opposite sign, characteristic of an oscillatory instability. This suggests that, despite each site being quasi-2D, it is the 1D physics that sets the dominant timescale. The stability of the soliton is increased when dissipation is added (see Appendix B).

IV. PHASE DIAGRAM

We now construct the full bistability phase diagram by numerically solving Eqs. (1), (2), and (4) using the TWA. As in the experiment, the dynamics are evaluated at the fixed time $t = 80$ ms, starting from two distinct initial conditions: one with an initially empty central site and another with a full central site. We use 251 lattice sites, which is sufficient to suppress finite-size effects for this timescale. Figure 4(a) shows the resulting atom number difference $|\Delta N|$ between these two initial conditions at the evaluation time, as a function of the tunneling J and dissipation γ. A large $|\Delta N|$ indicates sensitivity to initial conditions and thus signals bistability. For comparison, we overlay the experimental phase boundaries from Ref. [24]. Our simulations show excellent agreement with the experimental data at the upper boundary (large J), where the system transitions from a dark soliton to a uniform superfluid. Notably, this transition has not been accurately reproduced in previous theoretical studies except by unrealistically adjusting experimental parameters [27,62].

To highlight the role of the soliton, Fig. 4(b) displays the results of simulations with imposed mirror symmetry. Enforcing perfect in-phase driving from both sides leads to a conventional optical bistability [24,27,28], which predominantly affects the upper boundary of the bistable region. These soliton-free simulations predict an upper threshold at considerably *lower* J values than what is observed experimentally. While a lowering of the upper boundary can possibly be attributed to thermal and quantum fluctuations, it is much harder to account for an *increase* of the upper phase boundary. We therefore conclude that the spatial phase structure of the soliton was crucial to the observed bistability. Direct measurements of the relative phase would provide conclusive experimental confirmation of this mechanism.

Both phase diagrams differ significantly from the experimental data at the lower boundary. While theoretically this boundary is predicted to follow $J = \gamma/4$ [27,54] (white dashed lines), a much steeper linear relation, $J = \gamma$, was found experimentally. We attribute this discrepancy to finite-size and temperature effects. The experimental system in Ref. [24] only extended across ∼65 full sites, albeit not uniformly occupied due to the weak-harmonic confinement. The sound velocity $v = \sqrt{2Jd_z^2\mu}$ implies that over these timescales approximately 200 sites are needed to avoid finite-size effects. The dissipation could therefore have time to reduce the atom number of all sites substantially, lowering the interaction energy and making it easier to switch to the soliton state. Moreover, since an initial soliton state prevents substantial atom loss, the data at the upper boundary are far less affected by finite-size effects. In Appendix E, we confirm this by showing that the slope of the lower boundary increases with increasing fluctuations in the initial state, without substantially altering the agreement at the upper boundary.

V. CONCLUSION

We have uncovered a semiclassical first-order dark-state phase transition between a dark soliton and uniform superfluid state, which we used to quantitatively explain a phase boundary in a recent cold-atom experiment [24]. This result sheds light on these and other experimental observations [25,26], previously not understood from first principles. We demonstrated this through comparison with the mirror-symmetric system that displays a conventional optical bistability, but is in stark disagreement with the experimental results. The transition can be understood via Bogoliubov theory and with the 1D Bose-Hubbard model, for which our results confirm that the region of critical slowing down is substantially broadened for the soliton bistability (as is seen in the phase diagram) and the critical point is shifted to higher tunnel couplings.

Our results demonstrate that spatially extended coherent phase structures can fundamentally alter mean-field driven-dissipative transitions. Looking ahead, this mechanism suggests potential vortex-superfluid transitions in 2D, stabilization of phase structures via spatially patterned dissipation, and the use of dissipation as a phase switch for soliton imprinting [4,63–65] or for controlling superfluid flow [38]. Additionally, there are potential links to two-terminal superfluid and superconducting junctions, where transport properties are substantially modified by single particle loss [45].

ACKNOWLEDGMENTS

We thank M. Reeves and H. Ott for many useful discussions. R.C. and M.W. acknowledge the support of the Research Foundation-Flanders (FWO) through Project No. 39532, the HPC core facility CalcUA and the Flemish Supercomputer Center (VSC). S.E.B. acknowledges the support of the Young Scientist Training Program at the Asia Pacific Center for Theoretical Physics, and that this work was performed with support from the National Science Foundation (NSF) through Award No. OSI-2228725. M.J.D. acknowledges funding from the Australian Research Council (ARC) Centre of Excellence in Future Low-Energy Electronics Technologies (Project No. CE170100039) and an ARC Discovery Project (Project No. DP250102923).

DATA AVAILABILITY

The data that support the findings of this article are openly available [66].

APPENDIX A: TRUNCATED WIGNER APPROXIMATION AND SEMICLASSICAL EQUATIONS OF MOTION

We briefly discuss the derivation of Eqs. (1) and (2) via the Wigner phase-space formalism. We consider the dissipative Bose-Hubbard model described by the Lindblad master equation

$$\frac{d\hat{\rho}(t)}{dt} = -i[\hat{H}, \hat{\rho}(t)] + \hat{\Gamma}\hat{\rho}(t)\hat{\Gamma}^\dagger - \frac{1}{2}\{\hat{\Gamma}^\dagger\hat{\Gamma}, \hat{\rho}(t)\}, \quad \text{(A1)}$$

with Bose-Hubbard Hamiltonian

$$\hat{H} = -J\sum_j(\hat{a}^\dagger_{j+1}\hat{a}_j + \text{H.c.}) + \frac{U}{2}\sum_j \hat{a}^\dagger_j\hat{a}^\dagger_j\hat{a}_j\hat{a}_j, \quad \text{(A2)}$$

where $\hat{a}^\dagger_j$ and $\hat{a}_j$, respectively, denote bosonic creation and annihilation operators for site $j \in \{-L/2, L/2\}$ in a 1D chain of length $L+1$, and the particle loss on the central site is described by the jump operator $\hat{\Gamma} = \sqrt{\gamma}\hat{a}_0$. The parameter J is the nearest-neighbor tunneling amplitude and U is the on-site interaction energy. Equation (A1) can be represented in $2(L+1)$-dimensional phase space, where the Wigner function $W[\Psi, \Psi^*]$ is the analog of the density matrix. The Wigner distribution evolves according to

$$\frac{\partial W}{\partial t} = -i\sum_j\left(\frac{\partial}{\partial\psi_j}\mathcal{F}[\psi_j] - \text{c.c.}\right)W[\Psi, \Psi^*] + \frac{\gamma}{2}\frac{\partial^2}{\partial\psi_0\partial\psi_0^*}W[\Psi, \Psi^*] + \mathcal{O}(\partial^3), \quad \text{(A3)}$$

where

$$\mathcal{F}[\psi_j] = J(\psi_{j-1} + \psi_{j+1}) - U(|\psi_j|^2 - 1)\psi_j + i\frac{\gamma\delta_{0j}}{2}\psi_j. \quad \text{(A4)}$$

Neglecting third-order derivative terms, which vanish with $\mathcal{O}(1/N)$, this reduces to a Fokker-Planck equation that can be mapped to the Langevin Eqs. (1) and (2). This also implies an equation for the evolution of the local density n_j, which in the limit $N \to \infty$ on every site is given by

$$i\frac{d}{dt}n_j = -J(\psi_{j-1} + \psi_{j+1})\psi_j^* + \text{H.c.} - i\delta_{0,j}\gamma_j n_j, \quad \text{(A5)}$$

where $\psi_j = \sqrt{n_j}e^{i\phi_j}$. The dissipative contribution vanishes for a dark soliton [Eq. (3)], since $n_0 = 0$. The conjugate equation for ϕ_0 is irrelevant as this phase is purely a gauge due to the vanishing density. In addition, the dark soliton is an eigenmode of the remaining terms, i.e., the discrete Gross-Pitaevskii equation

$$i\hbar\partial_t\psi_j = -J(\psi_{j-1} + \psi_{j+1}) + U|\psi_j|^2\psi_j. \quad \text{(A6)}$$

The vanishing dissipation and eigenmode condition make the dark soliton a dark state of the Lindblad master equation in this limit.

APPENDIX B: LINEAR STABILITY ANALYSIS

1. One dimension

To determine the dynamical stability of the dark soliton in the dissipative Bose-Hubbard model, we analyze the eigenvalues of Bogoliubov excitations on top of the stationary dark soliton. The relevant equations are obtained by substituting the ansatz $\psi_j = \phi_j + \delta\psi_j(t)$ in Eqs. (1) and (2) and expanding the small perturbation as

$$\delta\psi_j(t) = \sum_l u_j^{(l)}e^{-i\omega_l t} + v_j^{(l)*}e^{i\omega_l^* t}. \quad \text{(B1)}$$

Here, $u_j^{(l)}$ and $v_j^{(l)}$ are the amplitudes of the lth normal mode with associated mode frequency ω_l. The resulting eigenvalue problem,

$$\begin{aligned}\omega_l u_{j,l} &= (-2J + 2U|\psi_j|^2 - \mu - i\gamma/2)u_{j,l} \\ &\quad + \psi_j^2 v_{j,l} - J(u_{j-1,l} + u_{j+1,l}), \\ \omega_l v_{j,l} &= (2J - 2U|\psi_j|^2 + \mu - i\gamma/2)v_{j,l} \\ &\quad - \psi_j^2 u_{j,l} + J(v_{j-1,l} + v_{j+1,l}),\end{aligned} \quad \text{(B2)}$$

is solved numerically, with ϕ_j given by Eq. (3). Two examples of the eigenvalue spectrum are depicted for values of J/γ above and below the critical point in Fig. 2. These clearly indicate the dynamically (un)stable nature of the dark state through the positive imaginary part of the individual modes.

Changes in the instability growth rate, $\max[\text{Im}(\omega_l)]$, as a function of dissipation rate γ are illustrated in Fig. 5. The solid lines represent the predictions of the incoherent pumping model introduced in Ref. [28] and show the swift decrease with an increasing dissipation rate. They clearly indicate, for a given tunneling strength J, a critical dissipation rate above which the dark soliton is rendered dynamically stable. These curves are complemented with results for finite Bose-Hubbard arrays [obtained via Eq. (B2)] with hard-wall boundaries of different lengths L, denoted by the broken lines. For very small $\hbar\gamma/\mu$, the different curves overlap, but eventually branch off. With increasing L, the growth rate curves also overlap with the solid lines up until larger values of γ/μ, indicating that the incoherent pumping model presented in Ref. [28] provides a plausible extrapolation to the thermodynamic limit. Furthermore, for a fixed dissipation rate in the intermediate regime of Fig. 5, the soliton lifetime, given by the

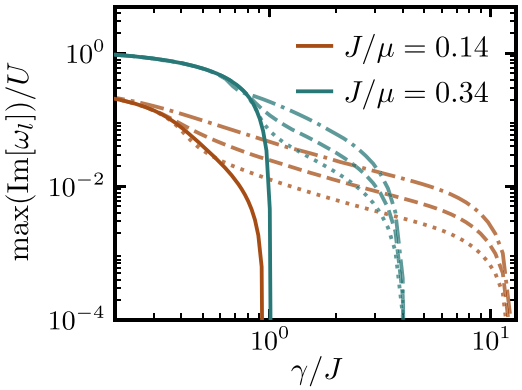

FIG. 5. Imaginary value of the pair of unstable modes as a function of relative dissipation strength γ/J (log-log scale). Different line styles indicate different system sizes, respectively, $L = 100$ (solid), $L = 200$ (dash-dotted), and $L = 400$ (dashed) for the full, dash-dotted, and dashed line. The dotted line illustrates the thermodynamic limit that was effectively realised with the incoherently pumped model introduced in Ref. [28].

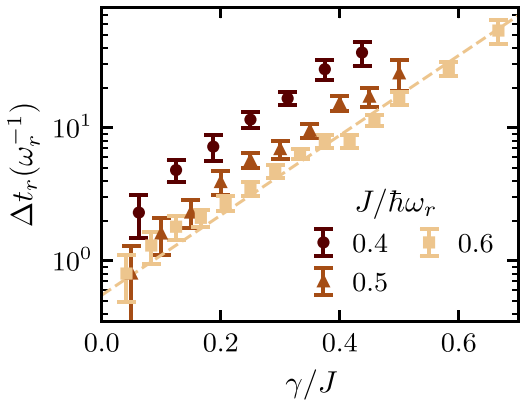

FIG. 6. Shifted relaxation timescale $\Delta t_r = t_r - t_r(\gamma = 0)$ as a function of relative dissipation strength γ/J, with fit $\Delta t_r \sim 10^{6.28\gamma/J}$. Dots indicate mean result from 10 samples and error bars indicate standard error. Results correspond to different J (legend), with $g_2 = 0.23\hbar\omega_r$ and $L = 100$. The state is initialized with $\Delta\Phi_0(0) \approx \pi$ with each half of the system in its ground state and an initial occupation on the central site of approximately 5%.

inverse of the instability growth rate, increases with growing system size L. Intuitively, for the finite-size systems, excitations created by the defect at the center of the chain cannot leave the system and are able to destroy the soliton state after multiple reflections from the hard-wall boundaries. This effect is reduced for larger chains. Notably, for large enough γ/μ, the instability is still suppressed for the finite-size systems.

2. Three dimensions

We now discuss the stability for the case of the quasi-1D chain, where each site is 2D. In the main text, Fig. 3 showed that starting from an initial state close to the soliton configuration, an oscillatory instability eventually leads to the erasure of the soliton, just as in the 1D case discussed above. These simulations were carried out in the absence of dissipation. We now show that dissipation increases the stability of the soliton. We define the corresponding relaxation time t_r as the first time in which the density on the central site exceed two-thirds of the value of a full site N_f, which indicates a significant departure from the soliton state in its evolution toward a "full" central site. This aligns with the definition of "filling time" in recent work by some of us [50] on unitary dynamics in a similar setup. Figure 6 shows t_r as a function of γ. It can be seen that the relaxation time diverges exponentially with γ as $\omega_r \Delta t_r = \omega_r[t_r - t_r(\gamma = 0)] \sim 10^{6.28\gamma/J}$, indicating that for fixed J the soliton becomes increasingly stable at higher dissipation rates due to the suppression of the oscillatory instability.

APPENDIX C: OPTICAL BISTABILITY

In the main text, we mention that the mirror-symmetric system possesses a conventional optical bistability. This follows from observations of Ref. [27], which developed a mean-field theory for the central site driven by a single undepletable coherent reservoir ψ_R and subject to dissipation. This is analogous to the situation in optical bistability of driven-dissipative Kerr resonators [18]. The equations of motion for the field ψ_0 are

$$i\hbar\frac{d\psi_0}{dt} = \mu\psi_0 + U|\psi_0|^2\psi_0 - 2J\psi_R - i\frac{\gamma}{2}\psi_0, \tag{C1}$$

where μ is the chemical potential on the central site. The steady-state solution possesses regions with one or three solutions; the latter being the bistable region. A pitchfork bifurcation occurs at the transition from one to multiple solutions. See Ref. [27] for additional details.

APPENDIX D: DETAILS OF EXPERIMENT AND SIMULATIONS

1. Experiment

As discussed in the main text, the experiment of Ref. [24] involved a one-dimensional chain of two-dimensional harmonic traps. Following an initial cooling process that produces the cigar-shaped bulk condensate, a one-dimensional optical lattice is applied with a depth of $s = 30\ E_r$ (where E_r is the lattice recoil energy), effectively isolating every site in a deep well for approximately 9 ms. During this preparation stage, the density on the central site can be independently adjusted relative to the rest of the system. To demonstrate bistability, two different initial states are distinguished. The local dissipation mechanism is either activated or left off during the preparation stage, leading to two possible scenarios: The trap at the center of the chain is either almost completely depleted or retains an occupation similar to the surrounding sites. Subsequently, the lattice is ramped down to a value within the range $s = 6$–$12E_r$, initiating the system dynamics. At this lower lattice depth the electron beam is turned on to provide a continuous source of particle loss.

The lattice spacing in the z direction is $a = 549$ nm and the radial trap frequency is $\omega_r = 165 \times 2\pi$ rad/s. The total number of Rb-87 atoms is 45×10^3, with mass

$m = 1.44 \times 10^{-25}$ kg and an s-wave scattering length $a_s = 5.8$ nm. Traps near the center of the chain contain approximately $N = 700$ atoms. The setup is harmonically trapped in the z direction as well, with $\omega_z \approx 10 \times 2\pi$ rad/s $\ll \omega_r$.

2. Simulation parameters and procedure

For our simulations, we neglect the slowly varying harmonic trap along the z axis and simulate a uniform lattice, as in our recent work in Ref. [50]. We begin with a first principles calculation of the corresponding lattice potential in the z direction, $V(z) = V_0 \sin^2(kz)$, where $k = 2\pi/\lambda$ is the lattice wavevector with wavelength $\lambda = 2a$ and spacing a. In the lowest band approximation, the on-site potential can be approximated as a harmonic oscillator, $V(z) \approx \hbar^2 \omega_{\rm lat}^2 z^2 / 4E_r$, where $E_r = \hbar^2 k^2/2m$ is the lattice recoil energy. Using the tight-binding approximation, the tunneling can be obtained as $J = \Delta E/4$, where ΔE is the bandwidth of the lowest-Bloch band [67], which we obtain by diagonalizing $\hat{H} = -\hbar^2 \partial_z^2/2m + V_0(2\pi z/\lambda)^2$ numerically. The tunnel coupling J and $\omega_{\rm lat}$ are in one-to-one correspondence and we restrict our attention to the experimentally relevant ranges [24].

For a given $\omega_{\rm lat}$, the interaction strength and chemical potential can be computed as follows. First, the 3D interaction strength is given by $g = 4\pi\hbar^2 a_s/m$. Due to the tight confinement in the z direction, we model this direction as discrete. The effective 2D interaction strength for each trap is given by numerically integrating over the Wannier function $w(z)$ in the z direction, i.e., $g_2 = g \int dz\, w(z)^4$. The chemical potential is then estimated as $\mu = \sqrt{g_2 m \omega_r^2 N/\pi}$ using the Thomas-Fermi approximation. This procedure uniquely determines $\omega_{\rm lat}$, g_2, and μ.

To find the ground state, we evolve the full chain in imaginary time. For the case in which the central site is initially full, this is taken as the initial condition. In contrast, for the complementary initial state, we decrease the atom number on the central site to 5% of its full value. As discussed in our recent work [50], the experimental preparation of the initially empty site introduces additional dephasing into the system. Specifically, both halves of the system are isolated from each other while the atom number is reduced on the central site. Reference [50] demonstrated numerically that the preparation stage is sufficiently long to allow significant diffusion of the relative phases. Moreover, once the lattice depth is lowered again, the empty site ensures that they cannot immediately "reconnect", thereby allowing additional time for diffusion. To capture this effect, for each Wigner trajectory, we multiply the right-hand subset of the chain, $R = \{j | j > 0\}$, by random phase $e^{i\theta}$, with $\theta \in [0, 2\pi]$. This phase randomization was shown in Ref. [50] to be necessary to achieve quantitative agreement with the experimental results of a comparable setup, albeit one governed by unitary dynamics. For the dissipative system the effect of this random phase is less significant. For the case of an initially full-site configuration, the choice of initial phase difference θ has no effect on the long-time results.

3. Simulation details

In this section, we provide a brief summary of the classical field (c-field) numerical methods employed in the main text. For the complete three-dimensional configuration, where each trap is modeled as a two-dimensional system, we need to restrict the number of modes per trap to satisfy the c-field approximation. This truncation is performed via the projection of the classical fields onto the coherent region $\mathcal{C}$, defined by

$$\mathcal{P}\{f(\boldsymbol{x})\} = \sum_{\boldsymbol{n}\in\mathcal{C}} \varphi_{\boldsymbol{n}}(\boldsymbol{x}) \int d^2\boldsymbol{x}' \varphi_{\boldsymbol{n}}^*(\boldsymbol{x}') f(\boldsymbol{x}'). \tag{D1}$$

Here, $\varphi_{\boldsymbol{n}}$ are eigenmodes of the cartesian Hermite-Gauss computational basis with quantum numbers $\boldsymbol{n} \in \{n_x, n_y\}$, which diagonalize the noninteracting problem ($g_2 = 0$). Letting $n = n_x + n_y$, we choose a cutoff $n_{\rm cut}$ to define the "classical field region" $\mathcal{C} = \{n \mid n_x + n_y \leqslant n_{\rm cut}\}$. This approach incorporates a consistent energy cutoff that limits the number of radial modes for each trap. In practice, we use a cutoff of approximately $n_{\rm cut} = 2.5\mu/\hbar\omega_r$. Previous works [27,50] have shown that results for this system are largely independent of the exact cutoff for $n_{\rm cut} > 2\mu/\hbar\omega_r$. This cutoff captures scattering processes in which two atoms at the chemical potential energy collide, leading to one atom with energy 2μ and another with approximately zero energy. This is anticipated to be relevant when the lossy site is significantly depleted, with an energy that is lower than neighboring sites by approximately μ. Atoms therefore cannot tunnel directly into the depleted condensate, but can undergo tunneling into excited states of the trap and relax via collisions.

Having defined a classical field region, the coupled projected Gross-Pitaevskii equations, displayed in Eqs. (1) and (2) in combination with Eq. (4), are integrated in the Hermite-Gauss basis using Gaussian quadrature [59,68]. For the simulations presented in the main text, the initial state is assumed to be a multimode coherent state $\psi_j(\boldsymbol{x}, 0) = \sum_{\boldsymbol{n}\in\mathcal{C}} \alpha_{j,\boldsymbol{n}} \varphi_{\boldsymbol{n}}(\boldsymbol{x})$, with the coefficients $\alpha_{\boldsymbol{n}}$ sampled from the phase-space distribution

$$W_c[\psi_j, \psi_j^*] = \left(\frac{2}{\pi}\right)^{|\mathcal{C}|} \prod_{\boldsymbol{n}\in\mathcal{C}} \exp\left(-2\left|\alpha_{j,\boldsymbol{n}} - \alpha_{j,\boldsymbol{n}}^{(0)}\right|^2\right), \tag{D2}$$

where $|\mathcal{C}|$ is the number of modes in the coherent region. Here, $\alpha_{j,\boldsymbol{n}}^{(0)}$ are the mean-field values obtained through imaginary time evolution for a given chemical potential. For a broader overview of c-field methods, see Ref. [59].

The numerical execution of the method is verified using two independent implementations, one coded in Julia [69] by the author R.C., and another using the XMDS [70] software. Both implementations yield identical results.

APPENDIX E: FINITE-SIZE AND TEMPERATURE EFFECTS

In this section, we demonstrate that the discrepancy with experimental results at the lower boundary of the phase diagram, shown in Fig. 4(a), could potentially be accounted for by additional fluctuations specific to the experimental setup. To mimic the effect of fluctuations due to a finite

temperature, we increased the variance on the distribution for the initial conditions in Eq. (D2). Formally, this does not correspond to a finite temperature, but still provides a qualitative picture of how the phase boundaries would change.

Figure 7 shows the bistability phase diagrams for the cases where the standard deviation of the initial distribution is multiplied by (a) 1.5 and (b) 2. Additionally, a smaller system with only 70 sites is simulated, in line with the experiment [24]. Notably, the largest change can be observed in the slope of the lower boundary. Enhanced fluctuations raise the lower boundary, but have no significant effect on the upper boundary, in agreement with observations in Ref. [27]. We conclude that the smaller system size in combination with fluctuations specific to the experimental setup causes the slope of the lower boundary to increase from the theoretical prediction of $J = \gamma/4$ [18,27] (white dash-dotted line) to approximate the observed $J = \gamma$ (blue dashed line). The upper boundary is less affected due to the robust nature of the dark soliton.

In addition, as discussed in the main text, the lower-boundary is expected to be far more sensitive to finite-size effects at a given time, since an initial soliton state prevents substantial atom loss as compared to the initially uniform superfluid state.

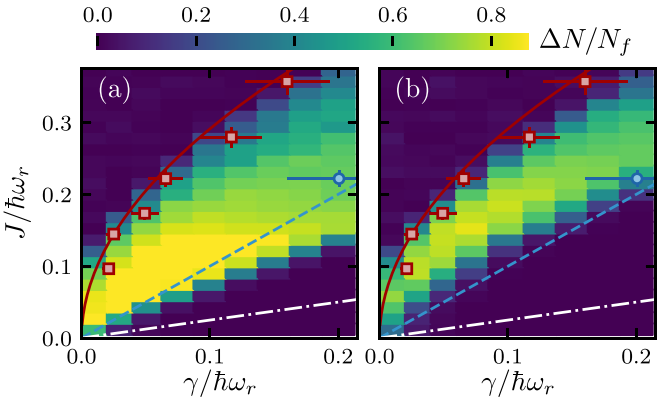

FIG. 7. Phase diagram in J-γ parameter space for $L = 70$, with increased uncertainty on initial state sampling as compared to the simulations in the main text: The standard deviation of the initial noise distribution is multiplied by (a) 1.5 and (b) 2. The color indicates the late-time (normalized) atomic population difference ΔN (legend) between simulations starting from different initial states: the empty and full central site, respectively. Displayed data correspond to $t = 80$ ms, averaged over 64 trajectories for each point. For comparison, the experimental phase boundaries from Ref. [24] are displayed with points and are fitted by $J \sim \sqrt{\gamma}$ (upper boundary) and $J \sim \gamma$ (lower boundary). The white dash-dotted line indicates $J = \gamma/4$ as expected from theory.

[1] S. Diehl, A. Micheli, A. Kantian, B. Kraus, H. Büchler, and P. Zoller, Quantum states and phases in driven open quantum systems with cold atoms, Nat. Phys. **4**, 878 (2008).

[2] F. Verstraete, M. M. Wolf, and J. Ignacio Cirac, Quantum computation and quantum-state engineering driven by dissipation, Nat. Phys. **5**, 633 (2009).

[3] J. T. Barreiro, M. Müller, P. Schindler, D. Nigg, T. Monz, M. Chwalla, M. Hennrich, C. F. Roos, P. Zoller, and R. Blatt, An open-system quantum simulator with trapped ions, Nature (London) **470**, 486 (2011).

[4] V. A. Brazhnyi, V. V. Konotop, V. M. Perez-Garcia, and H. Ott, Dissipation-induced coherent structures in Bose-Einstein condensates, Phys. Rev. Lett. **102**, 144101 (2009).

[5] J. Kasprzak, M. Richard, S. Kundermann, A. Baas, P. Jeambrun, J. M. J. Keeling, F. Marchetti, M. Szymańska, R. André, J. Staehli, *et al.*, Bose-Einstein condensation of exciton polaritons, Nature (London) **443**, 409 (2006).

[6] R. Ma, B. Saxberg, C. Owens, N. Leung, Y. Lu, J. Simon, and D. I. Schuster, A dissipatively stabilized Mott insulator of photons, Nature (London) **566**, 51 (2019).

[7] T. Tomita, S. Nakajima, I. Danshita, Y. Takasu, and Y. Takahashi, Observation of the Mott insulator to superfluid crossover of a driven-dissipative Bose-Hubbard system, Sci. Adv. **3**, e1701513 (2017).

[8] L. M. Sieberer, M. Buchhold, and S. Diehl, Keldysh field theory for driven open quantum systems, Rep. Prog. Phys. **79**, 096001 (2016).

[9] L. M. Sieberer, M. Buchhold, J. Marino, and S. Diehl, Universality in driven open quantum matter, Rev. Mod. Phys. **97**, 025004 (2025).

[10] M. Müller, S. Diehl, G. Pupillo, and P. Zoller, Engineered open systems and quantum simulations with atoms and ions Adv. At. Mol. Opt. Phys. **61**, 1 (2012).

[11] P. M. Harrington, E. J. Mueller, and K. W. Murch, Engineered dissipation for quantum information science, Nat. Rev. Phys. **4**, 660 (2022).

[12] M. Marcuzzi, E. Levi, W. Li, J. P. Garrahan, B. Olmos, and I. Lesanovsky, Non-equilibrium universality in the dynamics of dissipative cold atomic gases, New J. Phys. **17**, 072003 (2015).

[13] M. Buchhold, B. Everest, M. Marcuzzi, I. Lesanovsky, and S. Diehl, Nonequilibrium effective field theory for absorbing state phase transitions in driven open quantum spin systems, Phys. Rev. B **95**, 014308 (2017).

[14] D. Roscher, S. Diehl, and M. Buchhold, Phenomenology of first-order dark-state phase transitions, Phys. Rev. A **98**, 062117 (2018).

[15] J. Marino and S. Diehl, Driven Markovian quantum criticality, Phys. Rev. Lett. **116**, 070407 (2016).

[16] J. Marino and S. Diehl, Quantum dynamical field theory for nonequilibrium phase transitions in driven open systems, Phys. Rev. B **94**, 085150 (2016).

[17] S. E. Begg and R. Hanai, Quantum criticality in open quantum spin chains with nonreciprocity, Phys. Rev. Lett. **132**, 120401 (2024).

[18] P. D. Drummond and D. F. Walls, Quantum theory of optical bistability. I. Nonlinear polarisability model, J. Phys. A: Math. Gen. **13**, 725 (1980).

[19] S. Rodriguez, W. Casteels, F. Storme, N. Carlon Zambon, I. Sagnes, L. Le Gratiet, E. Galopin, A. Lemaître, A. Amo,

C. Ciuti, *et al.*, Probing a dissipative phase transition via dynamical optical hysteresis, Phys. Rev. Lett. **118**, 247402 (2017).
[20] E. M. Kessler, G. Giedke, A. Imamoglu, S. F. Yelin, M. D. Lukin, and J. I. Cirac, Dissipative phase transition in a central spin system, Phys. Rev. A **86**, 012116 (2012).
[21] D. Huybrechts and M. Wouters, Dynamical hysteresis properties of the driven-dissipative Bose-Hubbard model with a Gutzwiller Monte Carlo approach, Phys. Rev. A **102**, 053706 (2020).
[22] D. Roberts and A. A. Clerk, Competition between two-photon driving, dissipation, and interactions in bosonic lattice models: An exact solution, Phys. Rev. Lett. **130**, 063601 (2023).
[23] M. Foss-Feig, P. Niroula, J. T. Young, M. Hafezi, A. V. Gorshkov, R. M. Wilson, and M. F. Maghrebi, Emergent equilibrium in many-body optical bistability, Phys. Rev. A **95**, 043826 (2017).
[24] R. Labouvie, B. Santra, S. Heun, and H. Ott, Bistability in a driven-dissipative superfluid, Phys. Rev. Lett. **116**, 235302 (2016).
[25] J. Benary, C. Baals, E. Bernhart, J. Jiang, M. Röhrle, and H. Ott, Experimental observation of a dissipative phase transition in a multi-mode many-body quantum system, New J. Phys. **24**, 103034 (2022).
[26] M. Röhrle, J. Benary, E. Bernhart, and H. Ott, Dynamic hysteresis across a dissipative multi-mode phase transition, SciPost Phys. **16**, 158 (2024).
[27] M. T. Reeves and M. J. Davis, Bistability and nonequilibrium condensation in a driven-dissipative Josephson array: A c-field model, SciPost Phys. **15**, 068 (2023).
[28] R. Ceulemans and M. Wouters, Nonequilibrium steady states and critical slowing down in the dissipative Bose-Hubbard model, Phys. Rev. A **108**, 013314 (2023).
[29] G. Barontini, R. Labouvie, F. Stubenrauch, A. Vogler, V. Guarrera, and H. Ott, Controlling the dynamics of an open many-body quantum system with localized dissipation, Phys. Rev. Lett. **110**, 035302 (2013).
[30] A. Müllers, B. Santra, C. Baals, J. Jiang, J. Benary, R. Labouvie, D. A. Zezyulin, V. V. Konotop, and H. Ott, Coherent perfect absorption of nonlinear matter waves, Sci. Adv. **4**, eaat6539 (2018).
[31] M. Lebrat, S. Häusler, P. Fabritius, D. Husmann, L. Corman, and T. Esslinger, Quantized conductance through a spin-selective atomic point contact, Phys. Rev. Lett. **123**, 193605 (2019).
[32] H. Fröml, A. Chiocchetta, C. Kollath, and S. Diehl, Fluctuation-induced quantum zeno effect, Phys. Rev. Lett. **122**, 040402 (2019).
[33] M. Kunimi and I. Danshita, Nonequilibrium steady states of Bose-Einstein condensates with a local particle loss in double potential barriers, Phys. Rev. A **100**, 063617 (2019).
[34] D. Sels and E. Demler, Thermal radiation and dissipative phase transition in a BEC with local loss, Ann. Phys. **412**, 168021 (2020).
[35] H. Fröml, C. Muckel, C. Kollath, A. Chiocchetta, and S. Diehl, Ultracold quantum wires with localized losses: Many-body quantum Zeno effect, Phys. Rev. B **101**, 144301 (2020).
[36] Y. Yanay and A. A. Clerk, Reservoir engineering with localized dissipation: Dynamics and prethermalization, Phys. Rev. Res. **2**, 023177 (2020).
[37] T. Müller, M. Gievers, H. Fröml, S. Diehl, and A. Chiocchetta, Shape effects of localized losses in quantum wires: Dissipative resonances and nonequilibrium universality, Phys. Rev. B **104**, 155431 (2021).
[38] M. Will, J. Marino, H. Ott, and M. Fleischhauer, Controlling superfluid flows using dissipative impurities, SciPost Phys. **14**, 064 (2023).
[39] M.-Z. Huang, J. Mohan, A.-M. Visuri, P. Fabritius, M. Talebi, S. Wili, S. Uchino, T. Giamarchi, and T. Esslinger, Superfluid signatures in a dissipative quantum point contact, Phys. Rev. Lett. **130**, 200404 (2023).
[40] A.-M. Visuri, T. Giamarchi, and C. Kollath, Nonlinear transport in the presence of a local dissipation, Phys. Rev. Res. **5**, 013195 (2023).
[41] A.-M. Visuri, J. Mohan, S. Uchino, M.-Z. Huang, T. Esslinger, and T. Giamarchi, DC transport in a dissipative superconducting quantum point contact, Phys. Rev. Res. **5**, 033095 (2023).
[42] M. Gievers, T. Müller, H. Fröml, S. Diehl, and A. Chiocchetta, Quantum wires with local particle loss: Transport manifestations of fluctuation-induced effects, Phys. Rev. B **110**, 205419 (2024).
[43] M. Stefanini, Y.-F. Qu, T. Esslinger, S. Gopalakrishnan, E. Demler, and J. Marino, Dissipative realization of Kondo models, Commun. Phys. **8**, 212 (2025).
[44] J. Despres, L. Mazza, and M. Schirò, Dynamics of the Bose-Hubbard model induced by on-site or long-range two-body losses, arXiv:2502.09008.
[45] R. Ogino and S. Uchino, Anomalous supercurrents in the presence of particle losses, arXiv:2505.21085.
[46] R. Labouvie, B. Santra, S. Heun, S. Wimberger, and H. Ott, Negative differential conductivity in an interacting quantum gas, Phys. Rev. Lett. **115**, 050601 (2015).
[47] M. K. Olsen and J. F. Corney, Negative differential conductivity and quantum statistical effects in a three-site Bose-Hubbard model, Phys. Rev. A **94**, 033605 (2016).
[48] D. Fischer and S. Wimberger, Models for a multimode bosonic tunneling junction, Ann. Phys. **529**, 1600327 (2017).
[49] C. Mink, A. Pelster, J. Benary, H. Ott, and M. Fleischhauer, Variational truncated Wigner approximation for weakly interacting Bose fields: Dynamics of coupled condensates, SciPost Phys. **12**, 051 (2022).
[50] S. E. Begg, M. J. Davis, and M. T. Reeves, Nonequilibrium transport in a superfluid Josephson junction chain: Is there negative differential conductivity? Phys. Rev. Lett. **132**, 103402 (2024).
[51] G. Lindblad, On the generators of quantum dynamical semigroups, Commun. Math. Phys. **48**, 119 (1976).
[52] Y. S. Kivshar, W. Królikowski, and O. A. Chubykalo, Dark solitons in discrete lattices, Phys. Rev. E **50**, 5020 (1994).
[53] M. Johansson and Y. S. Kivshar, Discreteness-induced oscillatory instabilities of dark solitons, Phys. Rev. Lett. **82**, 85 (1999).
[54] P. D. Drummond and C. W. Gardiner, generalised P-representations in quantum optics, J. Phys. A: Math. Gen. **13**, 2353 (1980).
[55] T. Gericke, P. Würtz, D. Reitz, T. Langen, and H. Ott, High-resolution scanning electron microscopy of an ultracold quantum gas, Nat. Phys. **4**, 949 (2008).
[56] P. Würtz, T. Langen, T. Gericke, A. Koglbauer, and H. Ott, Experimental demonstration of single-site addressability in a

two-dimensional optical lattice, Phys. Rev. Lett. **103**, 080404 (2009).

[57] In Fig. 3(a), we subtract the mean phase at each time, evaluated using the circular mean, for ease of visibility; this removes the rapidly oscillating global phase. However, for an initial soliton configuration as in Fig. 3(b), the circular mean vanishes because the two domains differ by approximately π. In this case, we instead subtract by the average phase of the end sites, $(\Phi_{-L/2} + \Phi_{L/2})/2$, which centers the soliton's phase in each domain on $\pm\pi/2$, respectively. We then correct for trivial global π shifts that can flip these phases, i.e., $\pm\pi/2 \to \mp\pi/2$, from one time step to the next.

[58] P. B. Blakie and M. J. Davis, Projected Gross-Pitaevskii equation for harmonically confined Bose gases at finite temperature, Phys. Rev. A **72**, 063608 (2005).

[59] P. B. Blakie, A. S. Bradley, M. J. Davis, R. J. Ballagh, and C. W. Gardiner, Dynamics and statistical mechanics of ultracold Bose gases using c-field techniques, Adv. Phys. **57**, 363 (2008).

[60] N. Proukakis, S. Gardiner, M. Davis, and M. Szymańska, *Quantum Gases: Finite Temperature and Non-Equilibrium Dynamics* (Imperial College Press, London, 2013), Vol. 1.

[61] We define $\Delta\Phi_j = \Phi_{j+1} - \Phi_{j-1}$, where $\Phi_j = \langle\phi_{j+1}(\boldsymbol{x})\rangle_{\boldsymbol{x}}$, and the spatial average of the local phase $\phi_j(\boldsymbol{x})$ is conducted over a central region of site j.

[62] Reference [27] reproduced the experimental phase boundaries using fitted parameters. Their "multimode dynamical reservoir model" had two independent driving reservoirs, but also needed to use both (1) a chemical potential of $\mu = 12\hbar\omega_r$ instead of the experimental value of $7\hbar\omega_r$ and (2) a large effective temperature of $k_B T_{\rm eff} = 30\hbar\omega_r$ for the reservoirs. The relative phase between the reservoirs was not investigated.

[63] J. Denschlag, J. E. Simsarian, D. L. Feder, C. W. Clark, L. A. Collins, J. Cubizolles, L. Deng, E. W. Hagley, K. Helmerson, W. P. Reinhardt, S. L. Rolston, B. I. Schneider, and W. D. Phillips, Generating solitons by phase engineering of a Bose-Einstein condensate, Science **287**, 97 (2000).

[64] F. Trimborn, D. Witthaut, H. Hennig, G. Kordas, T. Geisel, and S. Wimberger, Decay of a Bose-Einstein condensate in a dissipative lattice—The mean-field approximation and beyond, Eur. Phys. J. D **63**, 63 (2011).

[65] C. Baals, A. G. Moreno, J. Jiang, J. Benary, and H. Ott, Stability analysis and attractor dynamics of three-dimensional dark solitons with localized dissipation, Phys. Rev. A **103**, 043304 (2021).

[66] R. Ceulemans, S. E. Begg, M. J. Davis, and M. Wouters, Data for Dark-state phase transition to a dark soliton in a dissipative Bose-Hubbard chain, Zenodo, 2026, doi:10.5281/zenodo.21396830.

[67] M. Arzamasovs and B. Liu, Tight-binding tunneling amplitude of an optical lattice, Eur. J. Phys. **38**, 065405 (2017).

[68] J. P. Boyd, *Chebyshev and Fourier Spectral Methods* (Dover Publications, New York, 2001).

[69] J. Bezanson, A. Edelman, S. Karpinski, and V. B. Shah, Julia: A fresh approach to numerical computing, SIAM Rev. **59**, 65 (2017).

[70] G. R. Dennis, J. J. Hope, and M. T. Johnsson, Xmds2: Fast, scalable simulation of coupled stochastic partial differential equations, Comput. Phys. Commun. **184**, 201 (2013).